

# Fiber-pigtailing quantum-dot cavity-enhanced light emitting diodes

L. Rickert,<sup>1</sup> F. Schröder,<sup>1</sup> T. Kupko,<sup>1</sup> C. Schneider,<sup>2,3</sup> S. Höfling,<sup>2</sup> and T. Heindel<sup>1,a)</sup>

<sup>1</sup>*Institut für Festkörperphysik, Technische Universität Berlin, 10623 Berlin, Germany*

<sup>2</sup>*Technische Physik, Physikalisches Institut, Wilhelm Conrad Röntgen Research Center for Complex Material Systems, Universität Würzburg, 97074 Würzburg, Germany*

<sup>3</sup>*Institut für Physik, Carl von Ossietzky Universität Oldenburg, 26129 Oldenburg, Germany*

a) Author to whom correspondence should be addressed. Electronic mail: [tobias.heindel@tu-berlin.de](mailto:tobias.heindel@tu-berlin.de)

We report on a process for the fiber-coupling of electrically driven cavity-enhanced quantum dot light emitting devices. The developed technique allows for the direct and permanent coupling of p-i-n-doped quantum dot micropillar cavities to single-mode optical fibers. The coupling process, fully carried out at room temperature, involves a spatial scanning technique, where the fiber facet is positioned relative to a device with a diameter of 2  $\mu\text{m}$  using the fiber-coupled electroluminescence of the cavity emission as feedback parameter. Subsequent gluing and UV curing enables a rigid and permanent coupling between micropillar and fiber core. Comparing our experimental results with finite element method simulations indicate fiber coupling efficiencies of  $\sim 46\%$ . The technique presented in this work is an important step in the quest for efficient and practical quantum light sources for applications in quantum information.

Solid-state based quantum-light sources are elementary building blocks for photonic quantum technologies [1-3]. Especially the maturity of single-photon sources (SPSs) based on semiconductor quantum dots (QDs) has advanced substantially in recent years [4,5], allowing for the efficient generation of quantum states of light under optical [6-9] or electrical pumping [10,11]. As a result, QD-based quantum light sources have been employed for many proof-of-concept experiments on quantum communication [12-14] and photonic quantum computing [15]. Most of these experiments, however, suffer from rather complex and bulky setups due to complex light extraction via free-space optics, hindering more widespread applications. On the other hand, the development of user-friendly devices for applications outside shielded lab environments recently attracted much interest [16,17]. A crucial aspect in this context concerns the direct coupling of the quantum light sources to optical single-mode (SM) fibers facilitating a robust packaging of the devices. Pioneering work in this direction utilized fiber-coupled QD samples employing fiber-bundles containing about 600 individual fiber cores to spatially post-select a single emitter [18]. More recently, the direct fiber-coupling of optically pumped photonic nanostructures with embedded QDs, such as photonic wires [19] and micropillars with oxide aperture [20], has been reported. The latter scheme has also been used to realize an optically pumped cavity-enhanced single-photon source with gates for spectral tuning of the QD emission [21]. In addition, optically-pumped fiber-integrated microcavities were employed for the generation of coherent acoustic phonons [22]. Moreover, schemes for the SM fiber-coupling of QD microlenses are currently under development using two-photon direct

laser writing of photonic microstructures [23]. While these previous efforts relied entirely on optically excited QDs, an electrically driven directly fiber-coupled QD device, not demonstrated to date, would clearly represent an important step in device integration towards efficient and practical quantum light sources.

In this work, we developed a technique enabling the direct and permanent coupling of electrically-pumped cavity-based quantum light sources to optical SM fibers. Our process exploits the emission of the cavity modes as direct feedback parameter for the precise relative alignment between cavity and fiber core. As all steps of this process can be carried out at room temperature, a simple setup can be used for its implementation.

The fiber-pigtailed device fabricated in this work is illustrated in Fig. 1(a). It comprises an electrically contacted QD micropillar cavity aligned with the core of a SM fiber (Thorlabs 780HP, core diameter  $d_{\text{core}} = 4.4 \mu\text{m}$ ) mounted in a ceramic ferrule (not shown in Fig. 1(a)) serving as larger contact area for the gluing step described further below. The micropillar cavity device itself is based on a cylindrical Fabry-Pérot resonator which is composed of an intrinsic  $\lambda$ -thick GaAs-cavity with a layer of self-organized InAs QDs in its center together with a lower n-doped and an upper p-doped distributed Bragg reflector (DBR).

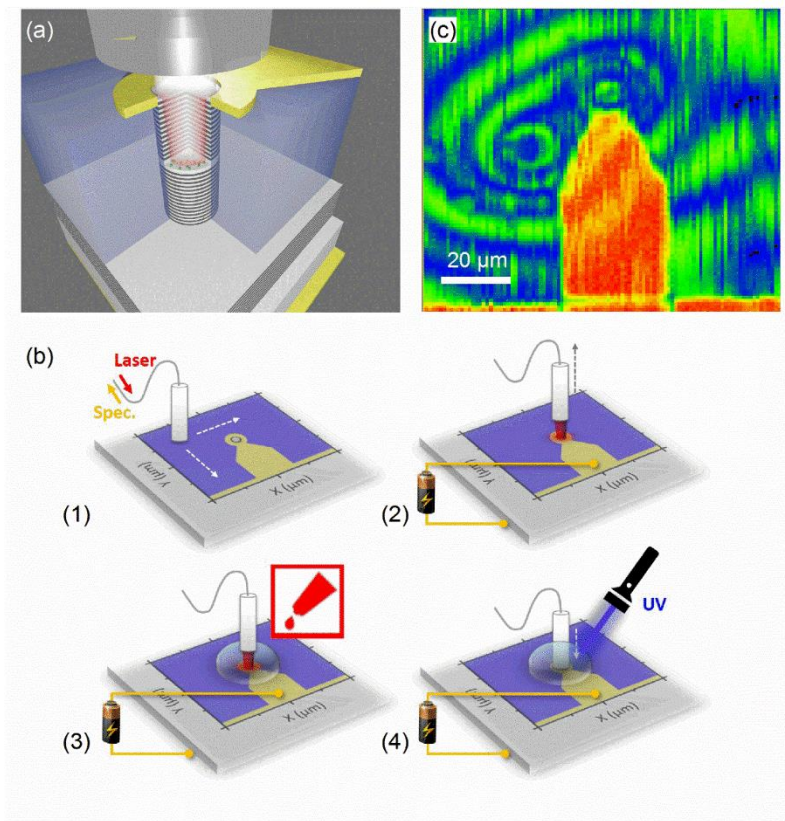


Figure 1. (a) Schematic representation of the fiber-pigtailed electrically contacted QD-micropillar. (b) Illustration of the fiber-coupling process conducted at room temperature: (1) scanning of the fiber-coupled laser signal to locate the target pillar, (2) precise fiber-to-pillar alignment via direct monitoring of the cavity's electroluminescence signal, (3) application of UV adhesive, and (4) UV curing using the cavity electroluminescence as feedback parameter. (c) Integrated intensity map of the reflected laser emission (spectral range:655-660 nm) of a  $100 \mu\text{m} \times 100 \mu\text{m}$  scan with  $1 \mu\text{m}$  step size during step (1) of the fiber-coupling process.

The number of the AlAs/GaAs mirror pairs is optimized for high photon extraction efficiencies resulting in moderate Q factors ( $\sim 1000$  to  $3000$ ) for devices of  $d_{\text{pillar}} = 2.0 \mu\text{m}$  diameter. The micropillar is planarized using Benzocyclobutene to support the ring-shaped electrical top contact, which is used for peripheral current injection together with a planar back contact. For details on the device design and the fabrication we refer the interested reader to Ref. [24]. For our fiber-coupling process presented in the following, we choose a small fiber ferrule with a diameter of  $1.25 \text{ mm}$  (standard size:  $2.5 \text{ mm}$ ) for two reasons: Firstly, the chip containing the target device can be made smaller, resulting in a larger yield of pigtailed devices per chip. Second, the distance between target device and the wire bond used for current injection can be shorter and damage of the wire bond during alignment of the ferrule is less probable.

For the precise coupling of the QD-micropillar to the SM fiber, we developed a robust four-step process fully performed under ambient conditions (i.e. room temperature, no vacuum) as sketched in Fig. 1(b). In step (1) the initial alignment of the fiber ferrule relative to the electrical contacts takes place using a laser-scanning method. Here, we detect the fiber-coupled emission of a diode laser ( $\lambda = 657 \text{ nm}$ ) after back reflection at the sample surface through a 90:10 fiber beam splitter using a spectrometer (10% excitation path, 90% detection path), while scanning the fiber facet across the sample surface using a 3D closed-loop piezo-stage. The resulting map of the integrated reflected intensity, exemplarily depicted in Fig. 1(c) for a micropillar with  $d_{\text{pillar}} = 4.0 \mu\text{m}$ , enables one to locate the top contacts as well as the top facet of a target micropillar. In step (2) the fiber core is precisely aligned with the micropillar to maximize the mode coupling by using the fiber-coupled cavity emission ( $\sim 900 \text{ nm}$ ) of the micropillar driven under direct current (dc) injection as feedback parameter. Compared to alignment under purely optical excitation, this procedure has the additional advantage, that the integrity of the electrical contacts can be monitored throughout the alignment process as well as the subsequent gluing and curing step. The height of the scanning fiber just before contact is adjusted by tracking the spectral position of the fundamental cavity mode, which shows a spectral blue-shift once the ferrule starts to strain the micropillar. In addition, the far-field emission properties of the QD micropillar can be studied during this step, as discussed further below (cf. Fig. 2). Step (3) concerns the application of optical UV-sensitive adhesive (NOA81,  $n = 1.56$ ): After maximizing the coupling of the cavity emission to the fiber mode, the fiber is lifted by about  $30 \text{ mm}$  normal to the sample surface, for applying the optical adhesive onto the sample using a syringe. Subsequently, the fiber is lowered again to its previous position. After once again optimizing the coupling between micropillar and fiber core, the UV curing process is started in step (4). Several exposure steps with increasing dose of collimated UV radiation (spot size  $9 \text{ mm}$ ) between  $10$  to  $160 \text{ mW/cm}^2$  were applied over several minutes to achieve complete curation of the adhesive. As mentioned earlier, the cavity emission is monitored during this process. After UV curing, the device is additionally encapsulated

using a two-component epoxide adhesive to further enhance the mechanical stability. The EL emission properties of the QD micropillar during and after the UV curing of the coupling process are discussed further below (cf. Fig. 3).

During the fiber-coupling process described above, the sample is mounted on a custom-made chip carrier with pin-connectors, bond pads for wire bonding, and a copper heatsink assuring thermalization of the micropillar sample for future operation at cryogenic temperatures. A coarse positioning of the micropillar device relative to the fiber is performed with an x-y-stage with a resolution of 1  $\mu\text{m}$ , while a 3D piezo-stage is used for fine positioning of the fiber ferrule with a resolution of better than 250 nm. Moreover, the fiber-to-micropillar distance can be coarsely adjusted with a z-stage (resolution: 1  $\mu\text{m}$ ). For electrical operation of the QD micropillar chip, we use a source measurement unit or a pulse pattern generator (300 ps minimal pulse-width, 250 MHz maximal repetition rate) for dc or pulsed current injection, respectively. The emission of the fiber-pigtailed microcavity is spectrally analyzed using a spectrometer with a spectral resolution of 25  $\mu\text{eV}$ .

For the final device, we choose a QD micropillar with a  $d_{\text{pillar}} = 2.0 \mu\text{m}$ , being the optimal trade-off between spectral QD density and photon extraction efficiency for this type of sample. Figure 2(a) shows a spectrum of the SM fiber coupled emission of the target device operated at room temperature and under dc injection ( $I = 16 \mu\text{A}$ , 5 s integration time). The spectrum was recorded during the alignment step (2) with the fiber facet being close to surface contact. Emission of the fundamental cavity mode ( $M_0$ ) at a wavelength of 905.8 nm as well as several higher order modes  $M_{1-3}$  are clearly visible. The far-field pattern of the  $M_0$ -mode is spatially resolved in the map shown in Fig. 2(b) displaying the fiber-coupled electroluminescence (FC-EL) of the integrated mode intensity. Figure 2(c) depicts the integrated FC-EL intensity of mode  $M_0$  extracted from the corresponding far-field patterns as a function of  $h$ . Here, we calibrated the origin of the  $h$ -axis to the point, at which the emission of a neighboring device started to show a blue-shift in the mode-spectra, indicating the point of physical contact. The integrated intensity decreases with increasing  $h$  due to the finite beam-divergence of the micropillar cavity, which will be investigated in detail further below. Pronounced oscillations are observed, which are due to the interference between the facets of micropillar and fiber core. This observation is in excellent quantitative agreement with the calculated mode coupling efficiency (gray line) obtained from finite element methods (FEM) simulations using the software package JCMSuite [25], assuming a dipole source at the center of the micropillar cavity. Note that we are not able to resolve the period of the interference fringes in our experiment, due to the limited resolution of the z-stage used (1  $\mu\text{m}$ ). To investigate the far-field emission properties of the micropillar cavity under study in more detail, we recorded FC-EL maps under fiber-coupled conditions as a function of  $h$ . From the recorded far-field patterns, we extracted the mode-field radius of the fundamental cavity mode  $M_0$  by fitting an elliptical 2D Gaussian function to the far-field data. For the data recorded at  $h = 2 \mu\text{m}$ , we extract mode-field radii of  $w_{x,\text{exp}} = (2.73 \pm 0.25) \mu\text{m}$  and  $w_{y,\text{exp}} = (2.96 \pm 0.27) \mu\text{m}$  in x- and y-direction, respectively. Considering the finite mode-field

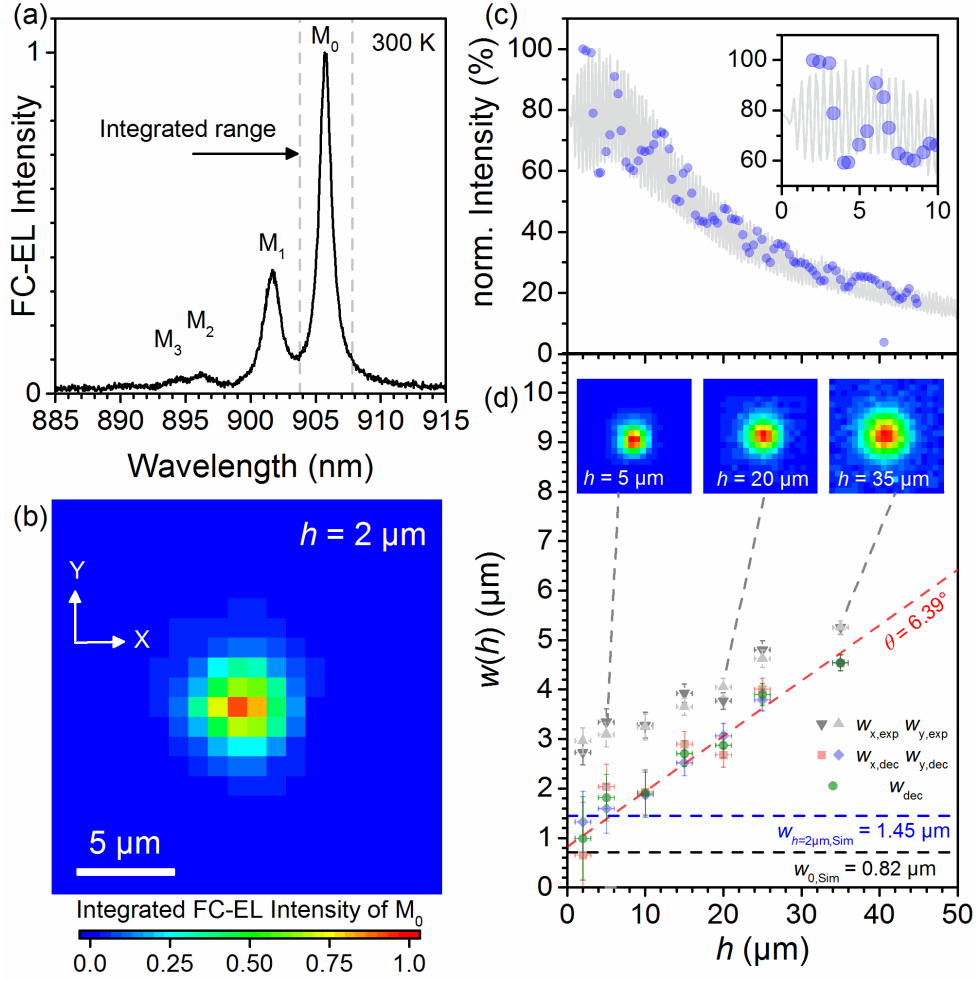


Figure 2. Investigation on the far-field emission of a QD micropillar ( $d_{\text{pillar}} = 2 \mu\text{m}$ ) directly coupled to a SM fiber before gluing. (a) Exemplary fiber-coupled electroluminescence (FC-EL) spectrum of the QD-micropillar operated under DC injection ( $I_{\text{dc}} = 16 \mu\text{A}$ ) at room temperature. (b)  $20 \mu\text{m} \times 20 \mu\text{m}$  far-field map of the integrated emission of the  $M_0$  mode at  $905.8 \text{ nm}$  collected through the SM fiber. (c) Measured FC-EL intensity of the  $M_0$  mode (blue dots) and simulated fiber mode coupling efficiency (gray line) as function of the fiber-to-pillar distance  $h$ . (d) Mode field radius  $w$  of the far-field emission of  $M_0$  as functions of  $h$ . Symbols refer to the far-field emission radius in x- and y-direction as measured (light/dark gray triangles) and deconvoluted with the fiber mode-field radius (red/blue squares). The horizontal dashed lines indicate mode radii obtained from FEM simulations at fiber-pillar distances  $h = 0$  and  $2 \mu\text{m}$ . The divergence angle  $\theta$  is extracted from the slope of the linear regression. Exemplary far-field emission patterns underlying the experimental data in (c) and (d) are shown between both subfigures for  $h = 5, 20$ , and  $35 \mu\text{m}$ .

radius of the fiber of  $w_{\text{fiber}} = 2.65 \mu\text{m}$  used to probe the far-field emission pattern, we obtain deconvoluted values according to

$$w_{\text{dec}} = \sqrt{w_{\text{exp}}^2 - w_{\text{fiber}}^2} \text{ of } w_{x,\text{dec}} = (0.66 \pm 1.06) \mu\text{m} \text{ and } w_{y,\text{dec}} = (1.32 \pm 0.61) \mu\text{m}. \text{ Here, the large errors cannot be avoided,}$$

due to the strong convolution of the mode-field radii of fiber and micropillar cavity. The deconvoluted mode radii as function of  $h$  are displayed in Fig. 2(d). Additionally, far-field EL emission intensity maps are displayed for  $h = 5, 20$  and  $35 \mu\text{m}$ .

The averaged value of  $w_{\text{dec}} = (w_{x,\text{dec}} + w_{y,\text{dec}})/2 = (0.99 \pm 0.84) \mu\text{m}$  at  $h = 2 \mu\text{m}$  lies well within the range expected from the FEM simulations, revealing a beam radius between  $w_{h=2\mu\text{m},\text{sim}} = 1.45 \mu\text{m}$  and  $w_{0,\text{sim}} = 0.82 \mu\text{m}$  at distances of at  $h = 2 \mu\text{m}$  and

0  $\mu\text{m}$ , respectively. The beam-divergence of fundamental mode is directly observed in Fig. 2(d), and we obtain a divergence angle  $\theta = (6.4 \pm 1.0)^\circ$  from the mode field radii ( $(3.7 \pm 0.7)^\circ$  from radius of half maximum). These values are somewhat smaller compared to the divergence angles reported in previous experimental reports on optically pumped micropillars of comparable size [26], a discrepancy that we explain by the differently structured devices (e.g. electrical ring-contact and different heights of the micropillar). From the values for the mode-field radii determined above, we can estimate the coupling efficiency to the SM fiber in our experiment as  $\eta = \left( \frac{2w_{\text{pillar}}w_{\text{fiber}}}{w_{\text{pillar}}^2 + w_{\text{fiber}}^2} \right)^2 \exp\left(-\frac{2u^2}{w_{\text{pillar}}^2 + w_{\text{fiber}}^2}\right)$ , where  $u$  denotes the transverse misalignment accounting for our positioning accuracy [27]. Assuming a deconvoluted pillar mode radii obtained from a radial symmetric 2D-Gaussian as  $w_{\text{pillar}} = (1.05 \pm 0.51) \mu\text{m}$ , we obtain an estimated value for the coupling efficiency of  $\eta = (46 \pm 33)\%$ , which lies again within the theoretically expected range of efficiencies between  $(31.45 \pm 0.83)\%$  and  $(69.96 \pm 0.80)\%$  at  $h = 0 \mu\text{m}$  and  $h = 2 \mu\text{m}$ , respectively, obtained with the simulated beam radii  $w_{0,\text{Sim}}$  and  $w_{h=2\mu\text{m},\text{Sim}}$  described above. Again, the large error in case of the efficiency estimation based on experimental parameters is caused by the large fiber mode-field used to probe the micropillar emission with a significantly smaller mode field.

Next, we proceed with step (4) of the fiber-coupling process to realize the permanently coupled fiber-pigtailed QD micropillar. As described in Fig. 1(b), we apply the optical adhesive and UV curing for this purpose. Figure 3(a) shows the FC-EL emission spectra with the cavity modes  $M_0$  and  $M_1$  recorded for monitoring the coupling efficiency before, during and after the curing of the UV adhesive. The applied UV dose displayed in Fig. 3(d) was increased stepwise from  $P_{\text{dose}} = 10 \text{ mW/cm}^2$  to  $160 \text{ mW/cm}^2$  during the 8 minutes curing period. During the  $10 \text{ mW/cm}^2$  dose period, adjustment steps indicated with an arrow in Fig. 3(a) are visible in the spectra, which were applied to optimize the fiber-coupling efficiency using the FC-EL signal as feedback parameter. Moreover, a comparison of the before- and after-curing spectra in Fig. 3(a) reveals a blue-shift of the cavity mode, which is observed with increasing UV dose during the curing process, accumulating to a spectral shift of about  $-0.5 \text{ nm}$  after curing is completed. This blue-shift, also observed in Ref. [19], can be explained by the strain exposed to the micropillar by the fiber-ferrule due to shrinkage of the optical adhesive during the UV curing process. Importantly, the magnitude of this shrinkage is not noticeably affecting the coupling efficiency of the device. After the UV curing step was successfully finished, the device was additionally encapsulated using epoxide adhesive. Comparing our curing process with the results reported by Haupt et al. in [19], we achieved a 14-times faster curing of our device combined with a negligible reduction in mode-coupling efficiency during curing. While the faster curing could be related to higher UV doses possible with our source based on collimated UV-LEDs, the noticeable degradation of the fiber coupling efficiency during curing in Ref. [19] might result from the larger mode-field of their device reacting more sensitive to misalignments relative to the fiber-mode.

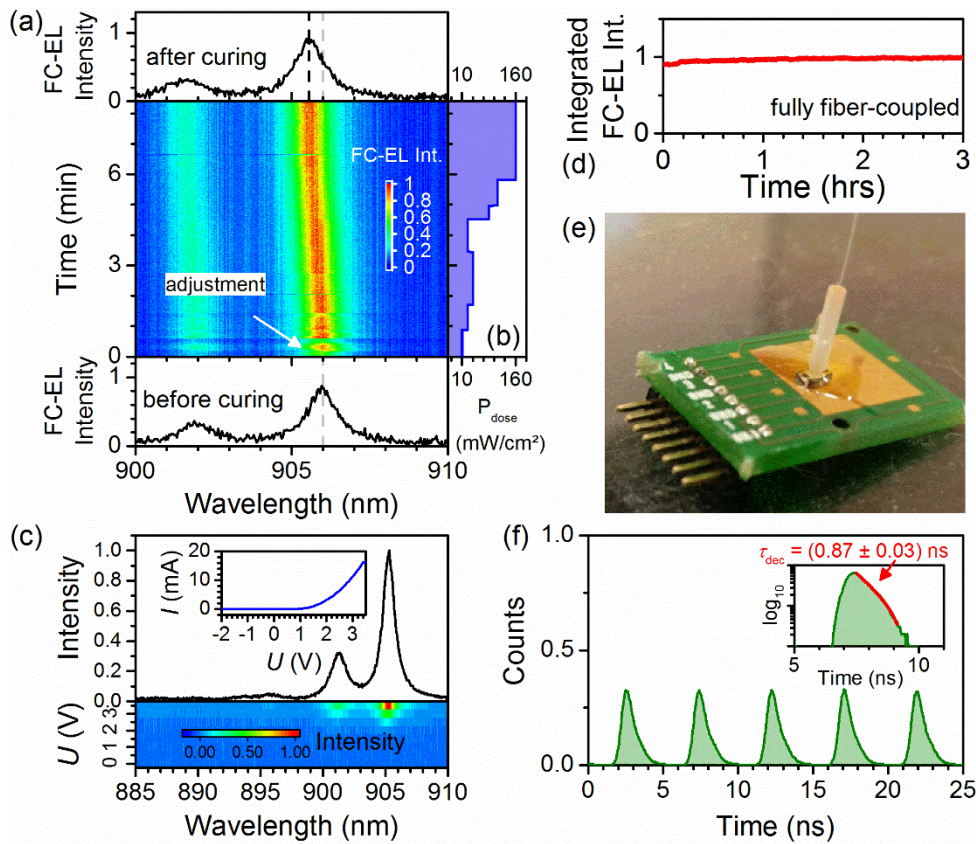


Figure 3. (a) FC-EL emission spectrum of the target micropillar at the beginning, during, and after the UV curing process and (b) used UV illumination doses  $P_{\text{dose}}$ . (c) FC-EL emission spectra of the fully fiber-coupled device after UV curing, with current voltage  $I$ - $U$ -characteristics as inset and FC-EL intensity versus excitation voltage. (d) Integrated FC-EL Intensity of the fully fiber-coupled device measured over three hours. (e) Exemplary fiber-coupled device. (f) Time-resolved EL emission data for pulsed excitation.

Next, we investigated the electro-optical properties of the permanently fiber-pigtailed micropillar device. Figure 3(c) presents the current-voltage characteristic of our fiber-pigtailed device under DC injection ( $\sim 16 \mu\text{A}$  per pillar) as well as the integrated FC-EL emission intensity of cavity mode  $M_0$ . The experimental data reveals a typical diode behavior of the fiber-pigtailed device, proving that the successful permanent coupling did not damage the wire bonds or the ring-shaped top-contact of the target device. An image of an exemplary fiber-coupled device is shown in Fig. 3(e). Finally, to proof the applicability of our device for applications requiring electronic triggering, we measure the temporal response of the FC-QDLED under pulsed current injection using a Silicon-based single photon counting module in combination with time-tagging electronics. The time-trace shown in Fig. 3(f) was recorded at an excitation repetition rate of 206.2 MHz, a pulse amplitude of 6.4 V, and a dc offset of 2.4 V. A periodic pulse train is observed with a decay time constant of 0.87 ns extracted from a mono-exponential fit to the falling pulse edge.

In summary, we developed a technique enabling the direct and permanent coupling of electrically-pumped cavity-based QD light emitting devices to optical SM fibers. The coupling process, fully carried out at room temperature, involves a spatial scanning technique, where the fiber facet is positioned relative to a device with a diameter of  $2.0\ \mu\text{m}$  using the fiber-coupled electroluminescence of the cavity emission as feedback parameter, ensuring maintained optimum fiber alignment throughout the whole process. Subsequent gluing and UV curing enables a rigid and permanent coupling between micropillar and fiber core. Comparing our experimental results with FEM simulations indicate fiber coupling efficiencies of  $\sim 46\%$  in our present device. This value is still limited by the non-ideal mode-field matching between micropillar and fiber-core, which can be substantially improved in future by either employing specialty fibers with smaller mode-field diameters or optimizing the layout of the QD-micropillar devices. A micropillar with diameter  $6.0\ \mu\text{m}$  exhibits a simulated mode-radius of  $2.54\ \mu\text{m}$ , yielding a fiber-coupling efficiency of  $\sim 99\%$  to the mode field of the given 780HP fiber. For a micropillar with  $d_{\text{pillar}} = 2.0\ \mu\text{m}$  and the experimentally observed mode field radius in this work, an available speciality fiber (UHNA3/Nuferm [28]) with a given mode field radius below  $1.3\ \mu\text{m}$  could be used, which yields coupling efficiencies of  $\sim 91\%$ . The technique for fiber-pigtailing cavity-enhanced QD light emitting diodes presented in this work is an important step in the quest for efficient and practical quantum light sources capable for high-speed electrical modulation [29] for applications in quantum information.

## ACKNOWLEDGMENTS

This work was financially supported by the German Federal Ministry of Education and Research (BMBF) via the project ‘QuSecure’ (Grant No. 13N14876) within the funding program Photonic Research Germany. Expert sample growth by M. Lermer as well as sample processing by M. Emmerling and A. Wolf is gratefully acknowledged. The authors further thank S. Reitzenstein for technical support of this project.

## REFERENCES

- [1] J. L. O'Brien, A. Furusawa, and J. Vučković, *Nat. Photonics* 3, 687 (2009).
- [2] I. Aharonovich, D. Englund, and M. Toth, *Nat. Photonics* 10, 631 (2016).
- [3] A. Acín et al., *New J. Phys.* 20, 80201 (2018).
- [4] S. Rodt, S. Reitzenstein, and T. Heindel, *J. Phys. Condens. Mat.* 32, 153003 (2020).
- [5] R. Trivedi, K. A. Fischer, J. Vučković, and K. Müller, *Adv. Quantum Technol.* 3, 1900007 (2020).
- [6] H. Wang et al., *Nat. Photonics* 13, 770 (2019).

- [7] S. Unsleber et al., *Opt. Express*. 24, 8539 (2016).
- [8] X. Ding et al., *Phys. Rev. Lett.* 116, 20401 (2016).
- [9] N. Somaschi et al., *Nat. Photonics* 10, 340 (2016).
- [10] Z. Yuan et al., *Science* 295, 102 (2002).
- [11] C. L. Salter et al., *Nature* 465, 594 (2010).
- [12] T. Heindel et al., *New J. Phys.* 14, 83001 (2012).
- [13] M. Anderson et al., *npj Quantum Inf.* 6, 1023 (2020).
- [14] T. Kupko et al., *npj Quantum Inf.* 6, 80201 (2020).
- [15] H. Wang et al., *Nat. Photonics* 11, 361 (2017).
- [16] A. Schlehahn et al., *Sci. Rep.* 8, 1340 (2018).
- [17] A. Musiał et al., *Adv Quantum Tech.* 3, 2000018 (2020).
- [18] X. Xu et al., *Appl. Phys. Lett.* 90, 61103 (2007).
- [19] D. Cadeddu et al., *Appl. Phys. Lett.* 108, 11112 (2016).
- [20] F. Haupt et al., *Appl. Phys. Lett.* 97, 131113 (2010).
- [21] H. Snijders et al., *Phys. Rev. Appl.* 9 (2018).
- [22] O. Ortiz et al., *Appl. Phys. Lett.* 117, 183102 (2020).
- [23] L. Bremer et al., *APL Photonics* 5, 106101 (2020).
- [24] T. Heindel et al., *Appl. Phys. Lett.* 96, 11107 (2010).
- [25] JCMwave GmbH, JCMSuite. The Simulation Suite for Nano Optics, 2021, <https://jcmwave.com/> - The mode coupling efficiency is calculated as fraction of a TE dipole source's total power coupling to the two-fold degenerate fundamental mode of the modeled SM fiber. The TE dipole is situated in the center of the micropillar, resembling a QD.
- [26] H. Rigneault, J. Broudic, B. Gayral, and J. M. Gérard, *Opt. Lett.* 26, 1595 (2001).
- [27] A. Ghatak and K. Thyagarajan, *Introduction to fiber optics* (Cambridge University Press, Cambridge, 1998).
- [28] Nufern, Ultra-High NA Single Mode Fibers, 2020, [https://www.nufern.com/pam/optical\\_fibers/spec/id/984/](https://www.nufern.com/pam/optical_fibers/spec/id/984/) - We point out that this fiber is specified for wavelengths of 960 nm or larger, making it not directly suitable for the emission wavelengths of the device used in this work. It emphasizes however, that technology is available for fibers with smaller mode fields, and we are of the opinion that it is sufficiently easy to either shift the device emission to larger wavelengths or use a similar fiber with slightly smaller wavelength requirements.
- [29] A. Schlehahn et al., *APL Photonics* 1, 011301 (2016)